Available online at www.sciencedirect.com
ScienceDirect
Trans. Nonferrous Met. Soc. China 31(2021) 3739−3751
Transactions of Nonferrous Metals Society of China
www.tnmsc.cn

Electrochemical dissolution and passivation of laser additive manufactured Ti6Al4V controlled by elements segregation and phases distribution

Jun YU[1,2], Tuo QIN[3], Xin LIN[1,2], Jun-jie WANG[1], Yu-feng ZHANG[1,2], Shi-yao WANG[1], Jing-yi YANG[1,2], Wei-dong HUANG[1,2]

1. State Key Laboratory of Solidification Processing, Northwestern Polytechnical University, Xi'an 710072, China;
2. Key Laboratory of Metal High Performance Additive Manufacturing and Innovative Design, MIIT, Northwestern Polytechnical University, Xi'an 710072, China;
3. Xi'an Microelectronic Technology Institute, The Ninth Academy of China Aerospace Science and Technology Corporation, Xi'an 710119, China

Received 31 December 2020; accepted 8 August 2021

Abstract: The electrochemical dissolution and passivation of laser additive manufactured Ti6Al4V were investigated through Tafel polarization, potentiostatic polarization and AC impedance measurements. The results show that the solution treatment−aging (STA) process aggravates the element micro-segregation compared to the annealing process, leading to varied Al and V contents of the phases from different samples. It is proven that either Al-rich or V-rich condition can highly affect the electrochemical dissolution behaviors due to thermodynamical instability caused by element segregation. The dissolution rate in the metastable passivation process is controlled by the stability of the produced film that is affected by phases distribution, especially the difficult-to-dissolve phase. And then, the dissolution rate of the phases in the transpassivation region is consistent with the rank in the activation process because the dense film is not capable of being produced. Compared to the annealed sample, the higher dissolution rate of the STA sample is beneficial to the electrochemical machining (ECM) of Ti6Al4V.

Key words: laser additive manufacturing; electrochemical dissolution behavior; microstructure characteristic; current efficiency; Ti6Al4V alloy

1 Introduction

Ti6Al4V is widely used for more than half output of various titanium alloy products. Thereinto, over 80% products are applied in the aerospace industry based on different fabrication techniques [1,2]. Laser additive manufacturing (LAM), a three-dimensional (3D) digital moldless, high-degree-of-freedom forming technology, is of advantages to satisfy aerospace application demands resulted from its feasibility on structure−function integration, complex-structure, lightweight, performance improvement and personalized implementation [3−5]. During the LAM of large-scale Ti6Al4V components, it is unavoidable to partly scarify forming accuracy in order to improve manufacturing efficiency. In this case, post-processing is taken a great concern because Ti6Al4V is a kind of difficult-to-cut material, which is prone to problems such as sticking and cold hardening. Moreover, the complexity of post-processing is increased once the machining allowance is highly limited in consideration of economic efficiency. Currently, the combination of high-efficient LAM and rapid electrochemical machining (ECM) based on the principle of anode dissolution, draws attention for hard-working

Corresponding author: Jun YU, Tel: +86-29-88494001, E-mail: yujun@nwpu.edu.cn; Xin LIN, E-mail: xlin@nwpu.edu.cn
DOI: 10.1016/s1003-6326(21)65710-2

materials to improve the efficiency and surface quality [6−9].

The researches on the corrosion resistance of forged titanium alloy have shown that the microstructure and element distribution can significantly change the electrochemical corrosion behaviors, and could further affect the electrochemical machinability and surface quality as well [10,11]. Compared to the forged titanium alloy, additively manufactured Ti6Al4V alloy has revealed stronger texture, coarser primary β grains and finer intragranular microstructure. It is reported that the as-fabricated selective laser melted (SLM) Ti6Al4V component shows worse corrosion resistance because its microstructure contains a large amount of metastable martensite phase and a low content of β phase [12], indicating that the phase constitution has a significant influence on the corrosion behavior. And LI et al [13] once studied the electrochemical corrosive anisotropy of the as-fabricated LAM Ti6Al4V, in which, the microstructure is composed of a large number of α plates and a small amount of β phase with inconsistent distributions on the vertical and horizontal planes, leading to the corrosive anisotropy. It is found that the vertical plane is less resistant to corrosion than the horizontal plane, providing a more friendly workability for electrochemical machining. Besides, the study on the relationship between the grain characteristic and electrochemical behavior of as-fabricated Ti6Al4V alloy shows that the equiaxed crystals are of slightly higher corrosion resistance than the columnar crystals due to the presence of texture, and degrade the corrosion resistance as the grain is coarsened [14]. Even some progress has been presented related to the corrosion performance of AM components focusing on the macro- or micro-structure distribution, the influence of elements segregation and phases distribution on the surface dissolution and passivation behavior has not been emphasized and studied carefully.

Moreover, the as-deposited LAM Ti6Al4V components need to be heat-treated to meet the requirement of engineering applications, by eliminating some issues such as uneven structure, residual stress and poor fatigue performance. The heat-treated components can generate a completely different structure and phase constitution through STA treatment [15−17]. In our previous study, the STA treated and annealed LAM Ti6Al4V components have a lower and a higher corrosion resistance compared to the annealed forged counterpart, respectively [18]. It is expected that some new micro-features related to structural morphology, phase distribution and element segregation altered by heat treatments, have vital influence on the electrochemical performance of heat-treated LAM Ti6Al4V alloy. Therefore, the effects of phases distribution and elements segregation on the anodic dissolution process and the passivation film stability are studied based on thermodynamical analysis for the heat-treated LAM Ti6Al4V alloy in the present work.

2 Experimental

2.1 LAM experiment

The LAM system consists of a 6 kW semi-conductor laser, a three-dimensional numerically-controlled working table, and a powder feeding system. The Ti6Al4V powders used are in a size range of 45−180 μm produced by plasma rotating electrode process (PREP) with a chemical composition (wt.%) of 6.16 Al, 4.06 V, 0.039 Fe, 0.12 O, 0.008 N, 0.005 H, and balance Ti. The powders were dried in a vacuum oven at 120 °C for 4 h and the substrate of a forged Ti6Al4V plate in a size of 140 mm × 60 mm × 10 mm was polished to remove oxide layer before the LAM process. A bulk sample in the size of 120 mm × 50 mm × 90 mm was fabricated in argon atmosphere glove box (oxygen content less than 5×10^{-5}) using a cross-hatching scanning strategy in the way of 90° shift between layers. The optimized processing parameters are listed in Table 1 and the applied heat treatments are stated in Table 2. The oxide layer after solution treatment and aging (STA) was removed and three cylindrical specimens at the same deposition height in a diameter of 15 mm and a height of 3 mm were prepared from the annealed and STA pieces, respectively. The machining

Table 1 Optimized LAM processing parameters

Power/kW	Spot diameter/mm	Scanning speed/(mm·min^{-1})	Powder feeding rate/(g·min^{-1})	Overlap ratio/%
2.35	5.0	900	25	50

Table 2 Samples and applied heat treatment regimes

Sample	Heat treatment
Annealed	Annealing at 550 °C for 4 h, and furnace cooling
STA890	Solution-treating at 890 °C for 2 h, and air cooling; aging at 550 °C for 4 h, and air cooling
STA920	Solution-treating at 920 °C for 2 h, and air cooling; aging at 550 °C for 4 h, and air cooling
STA950	Solution-treating at 950 °C for 2 h, and air cooling; aging at 550 °C for 4 h, and air cooling

surface of each sample is perpendicular to the deposition direction.

2.2 Sample preparation and analysis

The specimens were ground using abrasive paper, polished with SiO_2−H_2O_2 solution and then dried in flowing air for microstructural characterization and anodic polarization tests. The etching of specimens was done with an etchant consisting of 1 mL HF, 3 mL HNO_3, and 50 mL H_2O for 10 s for scanning electron microscopy (SEM), electron probe microanalysis (EPMA) and electron diffraction spectrometry (EDS). EDS was used to quantitatively analyze the elements distribution and the statistical analysis software Image-Pro Plus (IPP) was used to analyze the relative contents of the phases (area measurement method). The phases constitution was identified by X-ray diffraction with Cu K_α radiation (λ=1.5406 nm) with scanning step of 0.02° within 2θ range of 20°−100°. The areas of α and β diffraction peaks in the XRD spectra were determined by using the peak-fitting program, Fityk, with Pearson VII function. Then, the volume fractions (V_f) of α and β phases were calculated, respectively.

2.3 Electrochemical tests

The electrochemical tests were carried out in 15 wt.% NaCl solution at room temperature by using a PARSTAT 4000A electrochemical work-station in a conventional three-electrode cell. A platinum (Pt) sheet and a saturated calomel electrode (SCE) were used as the counter and the reference electrodes, respectively. All samples were loaded into an electrochemical test fixture as working electrode, whose area exposing to the solution was 1.0 cm^2. All the electrode potentials were referred to the SCE. The open circuit potential (OCP) was recorded to reach stable and the Tafel polarization tests were operated at a scan rate of 0.1667 mV/s ranging from −0.25 to +0.25 V relative to OCP. The AC impedance measurements were conducted in a frequency range between 100 kHz and 0.01 Hz using a sinusoidal potential perturbation of 10 mV in amplitude.

The potentiostatic polarization tests at 2, 3, 4 and 5 V (vs SCE) within the passivation region were carried out to investigate the dissolution and growth of passivation film. Before potentiostatic polarization tests, the potential of the working electrode was decreased to −1.0 V (vs SCE) for 10 min to remove air-formed oxide film from the surface, and then was increased gradually at a sweep rate of 25 mV/s. The passivation film was produced under the potentiostatic condition for 3 h to reach the steady state. The surface morphology of the samples was observed using a digital microscope after electrochemical testing.

3 Results

3.1 Microstructural characteristics

The microstructures after the annealing and STA treatments are presented in Fig. 1. The microstructure of the annealed sample is in the form of coarse columnar β composed of numerous α laths in some certain orientations and a small amount of β phase between α laths (Fig. 1(a)). After different STA treatments, the microstructure varies to the primary α laths (α_p) + transformed β (β_{trans}) colonies containing much finer acicular secondary α laths (α_s) in nano-scale (Figs. 1(b, c, d)). And the volume of β_{trans} colony is extended as the solution temperature is increased from 890 to 950 °C. Namely, the volume fraction of α_p is gradually reduced while that of the β_{trans} colony is increased, which is verified quantitatively in Table 3. Besides, the α_p laths show decreasing aspect ratio with the temperature increasing and approach the similar area to the β_{trans} colony at 950 °C (Fig. 1(d)). In addition, it is observed that the continuous grain boundary of α phase (α_{GB}) gets coarsened and even discontinuous for STA920 and STA950.

According to thermodynamic theory, the driving force of elements diffusion is originated

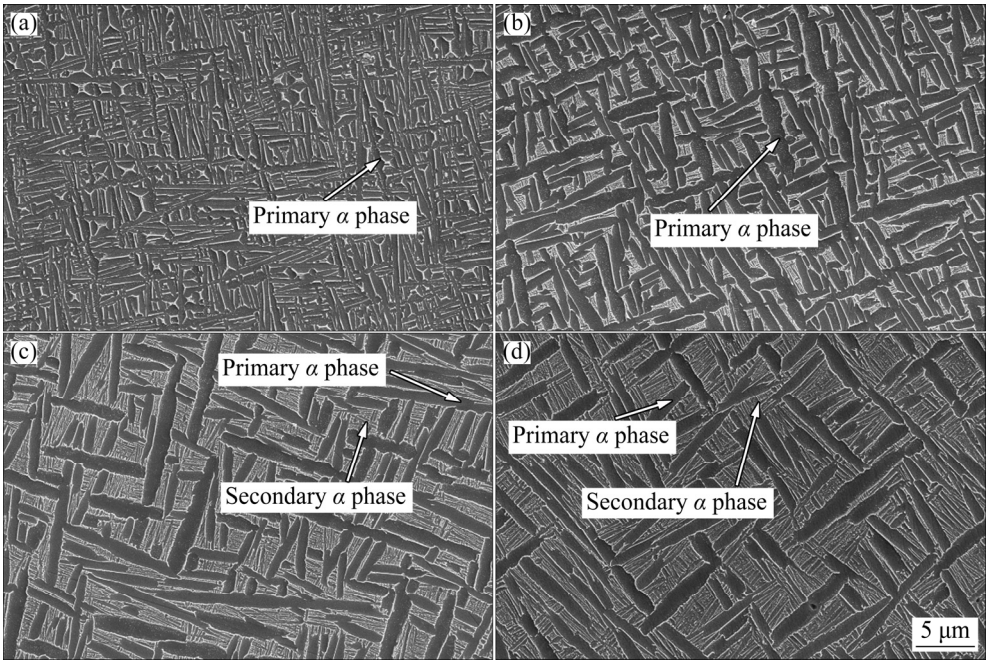

Fig. 1 Microstructures of different LAM Ti6Al4V samples: (a) Annealed; (b) STA890; (c) STA920; (d) STA950

Table 3 Characteristics of α_p phase for LAM Ti6Al4V samples

Sample	Width of α_p lath/μm	Volume fraction of α_p/%
Annealed	1.27±0.32	95
STA890	2.68±0.28	76
STA920	2.72±0.36	49
STA950	2.90±0.41	22

from the chemical potential disparity between the old and the new phases during phase transformation process. The solutes redistribution process is highly determined by the chemical compositions and the heat treatment regime. Figure 2 shows the EPMA results of the annealed and STA samples, which reveals a clear micro segregation of the solutes (Al and V) in the STA sample (Fig. 2(b)). In detail, the Al is basically segregated in the α_p, while V is in the β_{trans} colony. Moreover, the α_{GB} phase has relatively higher contents of Ti and Al, accompanied with a lowest V content compared to the intragranular structure. On the contrary, the β_{trans} colony is of a higher V content. It is noted that the elements distribution is much more uniform in the annealed sample (Fig. 2(a)), merely with a little low V content in the α_p. Thus, the STA treatment aggravates the micro segregation of the alloying elements Al and V along with the generation of β_{trans} colonies.

A quantitative analysis was carried out by EDS (Fig. 3). Within each sample, the Al content in different phases is in the order of $\alpha_{GB} > \alpha_{intra} > \beta_{trans}$, i.e., the α_{GB} is characterized to possess the highest Al content, followed by the intragranular α lath (α_{intra}) and β_{trans}. In comparison, the V content in different phases is in the sequence of $\alpha_{GB} < \alpha_{intra} < \beta_{trans}$. For different samples, the V content of α_{GB}, α_{intra} and β_{trans} keeps a monotonous decrease from the annealed to STA950, perfectly consistent with the increase tendency of the solution temperature. Unlikely, the monotonous increasing tendency of Al content for the α_{GB}, α_{intra} and β_{trans} is only fitted from the annealed, STA890 to STA920, and then changed to decrease for STA950. Therefore, among different heat-treated samples, the Al contents are in the order of annealed < STA890 < STA920 (> STA950), different from the vanadium tendency of annealed > STA890 > STA920 > STA950. It is highly expected that either Al- or V-rich condition could affect the electrochemical dissolution behaviors of different samples.

The XRD patterns of horizontal cross-sections of samples are shown in Fig. 4(a) marked with the corresponding crystal face indices. The samples present the same crystal faces except varied relative intensities. Surfaces (110), (102), (101), (103), (100) and (002) appear in a decreasing intensity order for the α phase and only (200) surface is identified for

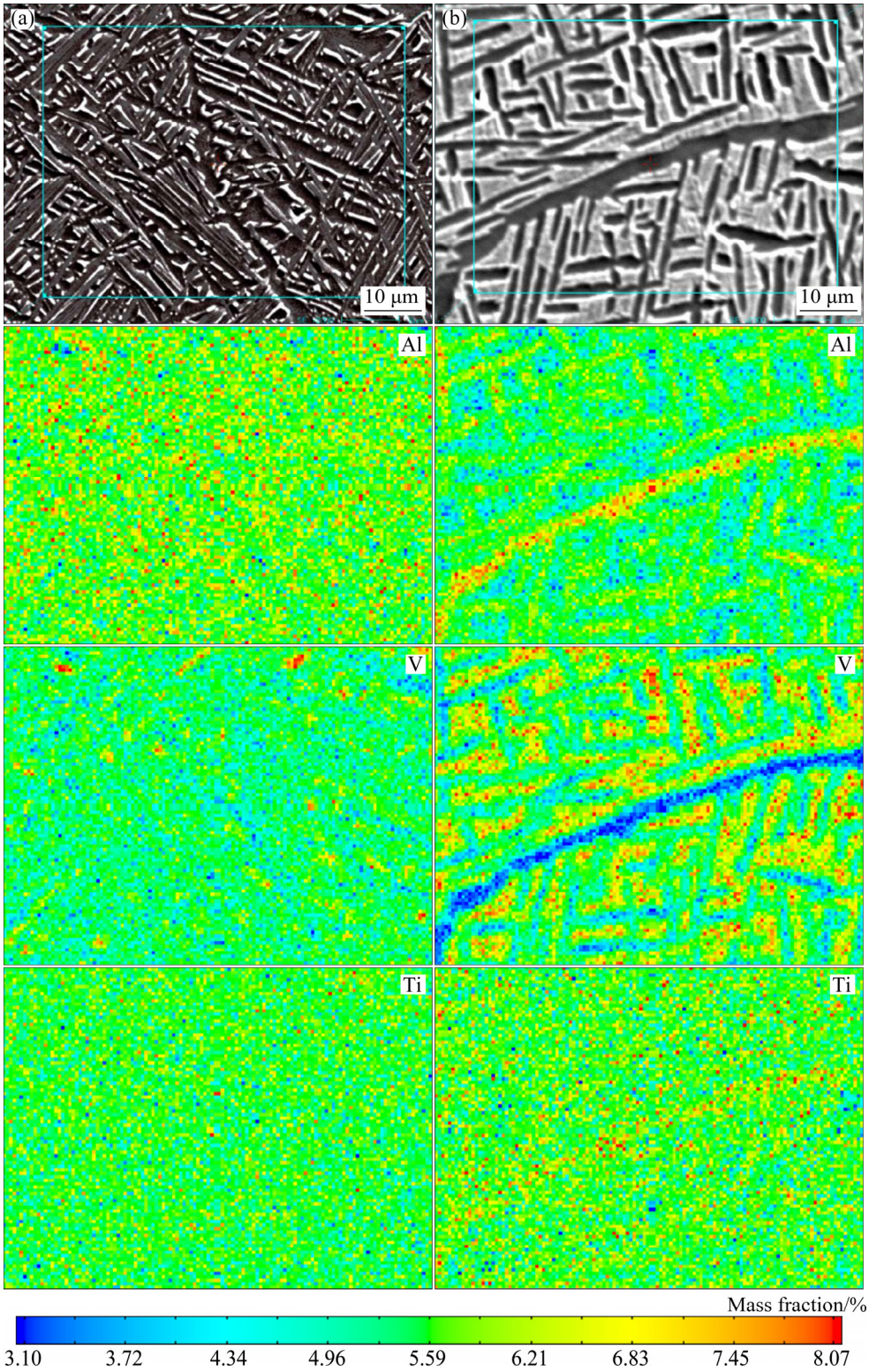

Fig. 2 EPMA mapping of annealed (a) and STA920 (b) samples

the β phase. The relative intensities vary significantly among different STA samples. The intensity of (102) is significantly improved for the samples of STA890 and STA920. However, the highest intensity for the STA950 sample shifts to (101) peak. According to the Pearson VII function and Fityk software, the volume fractions of β-phase are calculated to be 6.2%, 7.15%, 10.27% and 5.4% (Fig. 4(b)) for the annealed, STA890, STA 920 and STA 950 samples, respectively.

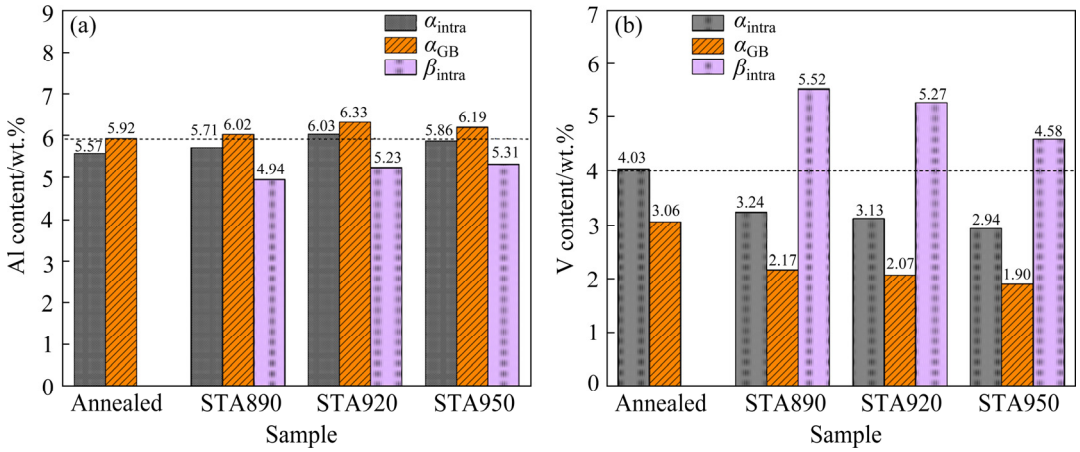

Fig. 3 Elements content in different samples: (a) Al; (b) V

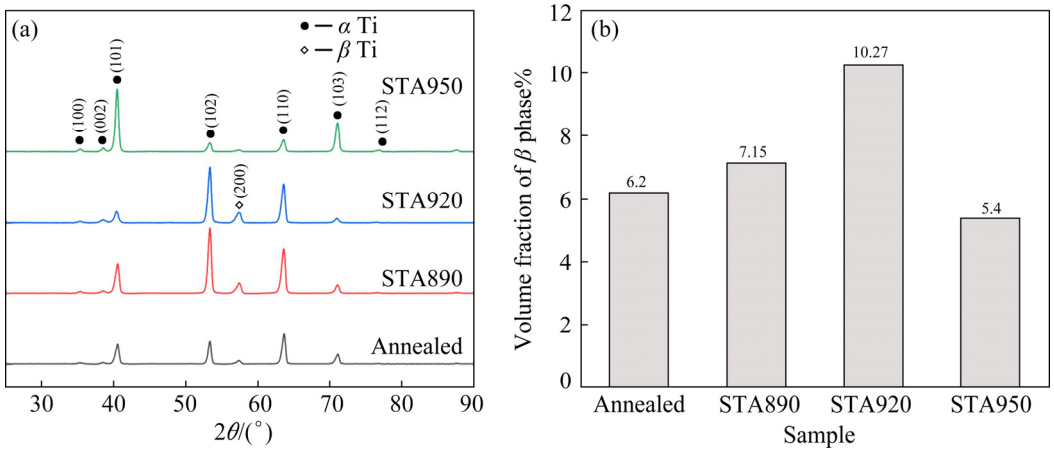

Fig. 4 XRD patterns of annealed and STA samples (a) and volume fraction of β phase in samples estimated from XRD pattern (b)

In order to understand the intensity variation of different surfaces, the surface energies of Ti (101), (102) and (110) were calculated based on the first-principles by introducing a pure Ti slab model according to Eq. (1):

$$E_{sur}=(E_{tot}-10E_{Ti})/S \quad (1)$$

where E_{sur}, E_{tot}, S and E_{Ti} are surface energy, total energy of slab model, sectional area of the slab and the energy of single Ti atom in bulk, respectively. The calculated surface energies show an order of (101) < (110) < (102) (Table 4). The (110) and (102) are easier to grow due to their relatively higher surface energies. The STA at 950 °C that is close to the phase transformation temperature activates the preferred orientation of (101) of β to α at a large volume fraction, leading to a peak shift for the STA950. In addition, the β volume fraction tends to rise first and then decrease. Therefore, the phase transformation of β to α is strengthened at 950 °C, in accordance with the fact that the preferred orientation of (101) is activated.

Furthermore, the lattice constants of α phase in the annealed and STA samples are calculated according to the distances between the corresponding diffraction crystal planes of the XRD results (Table 5). Both constants a and c of α phase increase firstly and then decrease with the solution temperature rising with a maximum for STA920. It is known that the lattice distortion depends on the solutes redistribution between α and β phases from

Table 4 Calculated surface energy of different Ti crystal planes

Crystal plane	E_{tot}/eV	E_{Ti}/eV	S/Å^2	E_{sur}/eV
(101)	−74.57	−7.84	15.56	0.12
(102)	−72.92	−7.84	20.22	0.13
(110)	−72.57	−7.84	23.65	0.12

Table 5 Calculated lattice parameters of α phase based on XRD patterns

Lattice parameter/nm	α-Ti	Sample			
		Annealed	STA890	STA920	STA950
a	0.295	0.29234	0.29246	0.29271	0.29255
c	0.468	0.46387	0.46476	0.46611	0.46522

high temperature, which is quite sensitive to the concentration of V element because of its much smaller atomic radius (1.35 Å) compared to Ti (1.45 Å) and Al (1.43 Å). Therefore, the lattice constants could decrease with the increase of the concentration of V and Al elements compared to pure Ti. Moreover, the calculated values of a and c based on XRD results basically rely on the phase in majority, which is the primary α phase for the annealed, STA890 and STA920 samples, and the secondary α phase (up to 78 vol.%) in β_{trans} for the STA950 sample. The content of V in the primary α phase keeps an increasing tendency from STA920, STA890 to the annealed sample, leading to a progressive lattice contraction. For the STA950 sample, its lattice constants decrease as well compared to the STA920 under the effect of the higher V content in β_{trans} and the lower V content in the primary α. Besides, the calculated a and c values of STA samples are higher than those of the annealed sample, illustrating that the lattices are expanded mainly due to the micro-segregation of the elements.

3.2 Electrochemical dissolution characteristics

The electrochemical dissolution behaviors of the heat-treated LAM Ti6Al4V alloy with different microstructures are studied. The curves of potential versus time at the open circuit condition in 15 wt.% NaCl solution are shown in Fig. 5(a). The curves start with an instant upward trend, and then gradually reach stable state in about 2 h, where the annealed sample shows the highest OCP of −205 mV representing the best corrosion resistance, followed by the STA890, STA920 and STA950 with the OCPs of −221, −257 and −268 mV, respectively. Figure 5(b) shows the Tafel curves with the polarization potential scanning from below the OCP in positive direction. Each sample was tested three times and the results show a good repeatability. The self-corrosion potentials (φ_{corr}), self-corrosion currents (I_{corr}), cathode Tafel slopes (β_c) and anode

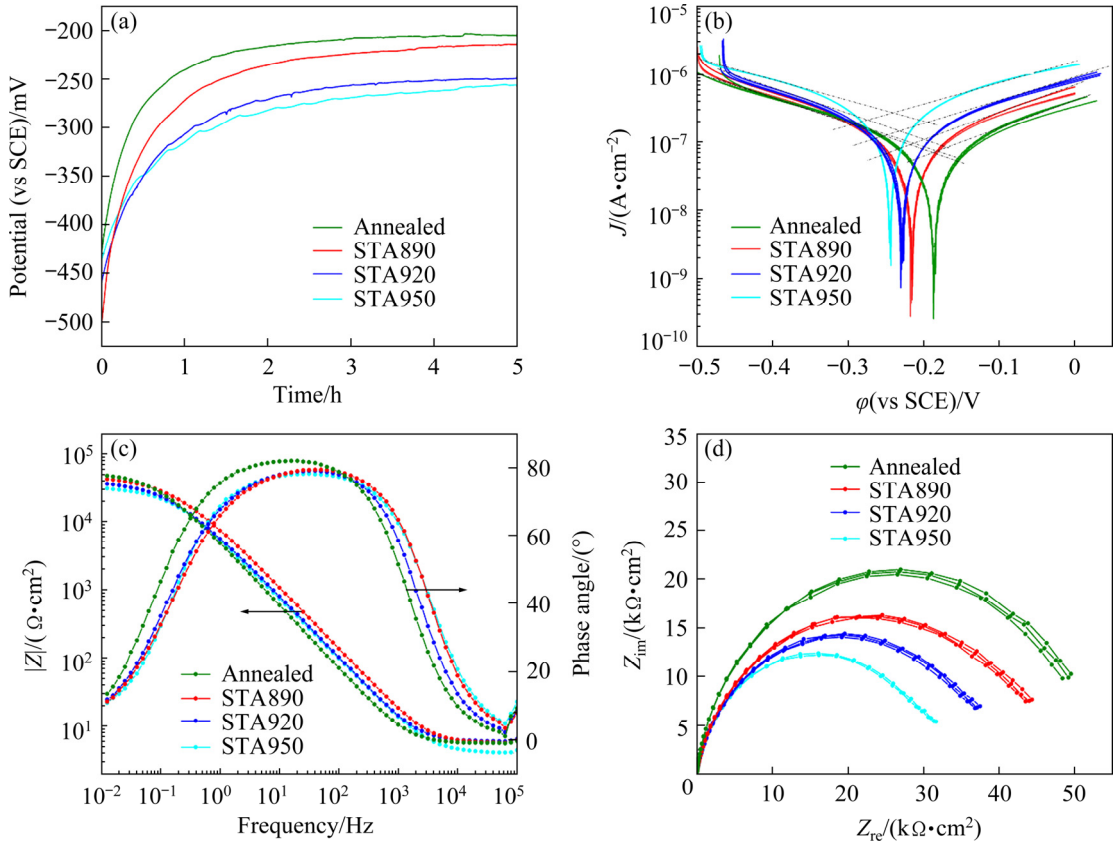

Fig. 5 OCP (a), Tafel curves (b), Bode (c) and Nyquist (d) plots for samples in 15 wt.% NaCl solution

Tafel slopes (β_a) are deduced in Table 6. It is revealed that the φ_{corr} values can be improved following the rank order of STA950, STA920, STA890 and annealed sample, accompanied with a monotonous decreasing tendency of the I_{corr} from around 0.832 to 0.162 μA. According to Faraday's law [19], the I_{corr} and corrosion rate v_{corr} follow the following relationship:

$$v_{corr} = \frac{I_{corr} K E_W}{\rho} \quad (2)$$

where E_W, K and ρ are the electrochemical equivalent, constant and density of corroded metal, respectively. For alloy with a given composition, the value of v_{corr} is positively proportional to that of I_{corr}. Therefore, the corrosion rate degrades in accordance with the order of STA950 > STA920 > STA890 > annealed sample.

Figures 5(c, d) show the results of electrochemical impedance spectroscopy (EIS) of the annealed and STA samples in OCP condition. The impedance moduli and the phase angles for all the samples vary in similar manner with the frequency increasing (Fig. 5(c)). All the samples represent a high-capacitance characteristic by exhibiting high phase angle close to 90° at the low and medium frequencies, together with the representation of the semicircle-like arc (Fig. 5(d)). It is proven that passivation film is formed on the surface in the 15 wt.% NaCl electrolyte. Relatively, the impedance moduli decrease quickly from a maximum at a low frequency of 0.01 Hz to a constant at high frequencies, which reflects the electrolytic solution resistance as reported [20]. Being of the highest phase angle and impedance modulus at the lowest frequency of 0.01 Hz, the annealed sample produces much more stable passivation film leading to the lowest I_{corr} as shown in Fig. 5(b) and Table 6.

Figure 6 shows the anode polarization curves of the samples in NaCl solution. All the samples perform active dissolving (Region I), metastable passivation (Region II) to over-passivation dissolving (Region III) processes by enhancing potential up to 9 V. It is illustrated that the annealed sample has the smallest passivation current slowly rising from the initial current of 9.148 μA/cm^2 to the breakdown current of 691.75 μA/cm^2. The curves of STA890 and STA950 approach closely as currents vary from 22.7 to 725 μA/cm^2 for the former and from 15.4 to 730 μA/cm^2 for the latter. The STA920 sample shows the highest passivation and over-passivation initial currents, rising from 24.9 to 972 μA/cm^2. The potential and current to initiate the over-passivation dissolution process can provide an important reference for electrochemical machining. In addition, a metastable re-passivation phenomenon (the zig-zag fluctuations) for the STA sample in the over-passivation region is observed. As the over-passivation dissolution occurs at the pitting point located at α_p phase, the dissolution can be blocked during its extension to the surrounding β_{trans} phase. Thus, a large number of lysates can be locally deposited resulting in re-passivation phenomenon until the reaction center is dissolved violently under the effects of the increased potential and the adjacent pitting points.

The samples were subjected to potentiostatic polarization tests at 2, 3, 4 and 5 V (Fig. 7), in which the currents are increased exponentially as the polarization potential is enhanced. This indicates that the passivation films are dissolved distinctly in acceleration. The highest steady-state polarization current at different polarization potentials is revealed for the STA920 sample, followed by the samples of STA890 and STA950. And the lowest polarization current is obtained from the annealed sample, which proves that a more stable passivation film exists. Correspondingly, the moduli of passivation films at 0.01 Hz in Fig. 7(b) show the highest and the lowest data for the annealed and STA920 samples, respectively. Besides, the moduli decrease by more than one

Table 6 Tafel polarization analysis for annealed and STA samples

Sample	φ_{corr}/mV	I_{corr}/μA	β_c/mV	β_a/mV
Annealed	−182.242±2.1	0.162±0.025	438.713	402.995
STA890	−217.499±1.8	0.172±0.023	354.988	397.242
STA920	−230.807±2.6	0.236±0.032	439.976	500.987
STA950	−256.886±3.0	0.832±0.028	763.226	806.598

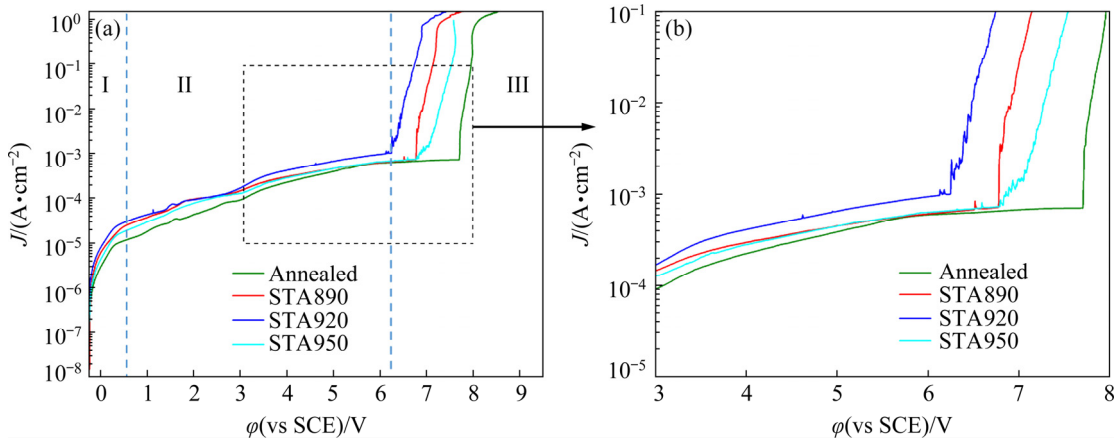

Fig. 6 Potentiodynamic polarization curves of annealed and STA samples in 15 wt.% NaCl solution

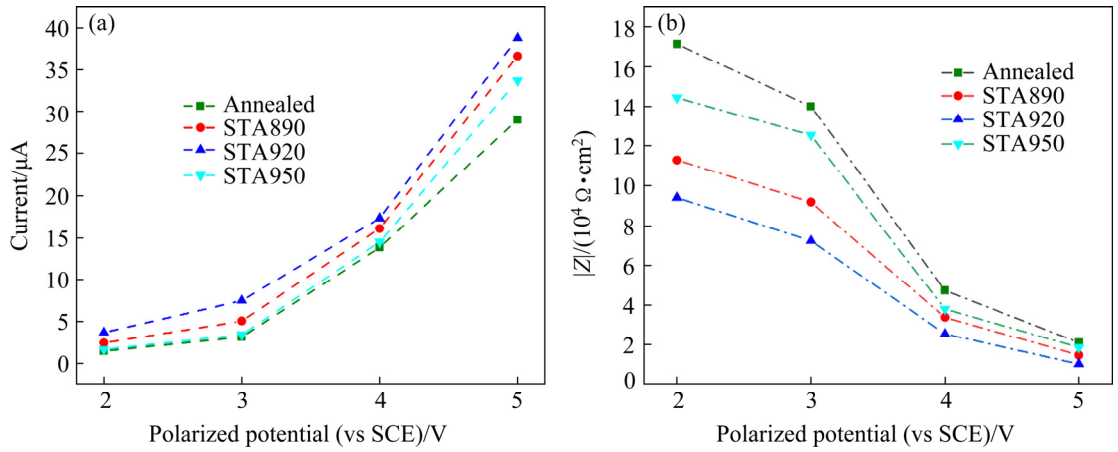

Fig. 7 Potentiostatic polarization modulus for annealed and STA samples: (a) Current; (b) $|Z|$

order of magnitude with the increase of polarization potential. The difference of $|Z|$ between lines reaches the minimum at 5 V, which reveals that the difference from the passivation films can be eliminated as the polarization potential increases.

4 Discussion

4.1 Corrosion performance in metastable passivation region II

It was reported that the passivation film formed on titanium alloy is generally composed of a porous loose outer layer and a dense inner layer providing key protection [21]. A two-layer equivalent circuit model (Fig. 8) is proven to fit very well with the EIS data of Fig. 5 according to the small Chi-square values (χ^2) data listed in Table 7. The R_{el} refers to the electrolytic solution resistance. For each sample, the value of $Z_{CPE(2)}$ of dense inner layer is slightly higher than the value of $Z_{CPE(1)}$ of porous outer layer, accompanied with a significant higher R_2 than R_1.

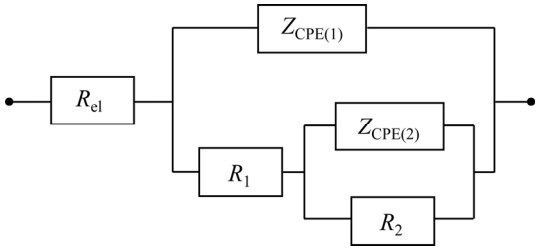

Fig. 8 Fitted equivalent circuit model based on EIS data

The calculated values of R_2 and R_1 show a downward trend with the increase of the heat-treated solution temperature. Besides, the value of n_2 being near to 1 indicates that the inner layer approaches to a pure capacitance, which is consistent with the statement of high phase angles of Fig. 5(c). Therefore, the inner layer of the passivation film dominates the electrochemical reaction and determines the stability of passivation film.

Under condition of potentiostatic polarization at 2−5 V, the parameters listed in Table 7 are shifted into the data of Fig. 9. For each sample, the value of

R_2 keeps a distinct drop between 2 and 4 V and reaches stable at 5 V in the range of 2−3 kΩ/cm^2 (Fig. 9(a)). Among the samples, the value of R_2 follows the order of STA920 < STA890 < STA950 < annealed sample. In addition, the decrement of $Z_{CPE(2)}$ from 2 to 5 V (Fig. 9(b)) follows the order of STA920 > STA890 > STA950 > annealed sample as well. Therefore, much severe electrochemical reactions occur for STA920, leading to an intensified dissolution behavior on its inner layer of the passivation film. Differently, both the values of R_1 and $Z_{CPE(1)}$ show an oscillation mode (Figs. 9(c, d)) attributed to a competition between lysate deposition and peeling behavior on the porous outer layer.

The different performances of the passivation films are closely related to the element and phase distributions including the phase volume fractions after different heat treatments. Compared to the STA samples, a basket-like structure of the annealed sample with the lowest volume fraction of β phase and the most uniform element distributions is beneficial to generating dense and uniform passivation film with the highest R_2 (Fig. 9(a)). However, the β_{trans} colonies of STA samples in the form of acicular α_s+β structure sacrifice the overall corrosion resistance to a certain extent by introducing a large number of α_s/β micro-batteries. Thereinto, STA920 sample contains the maximum volume fraction of β phases (Fig. 4(b)), leading to the most unstable passivation layer due to the dissolution-rate difference between α and β,

Table 7 Fitted parameters based on EIS data for annealed and STA samples at OCP

Sample	R_{el}/ ($\Omega\cdot cm^{-2}$)	$Z_{CPE(1)}$/ ($S\cdot s^n\cdot cm^{-2}$)	$Z_{CPE(2)}$/ ($S\cdot s^n\cdot cm^{-2}$)	n_1	n_2	R_1/ ($\Omega\cdot cm^{-2}$)	R_2/ ($\Omega\cdot cm^{-2}$)	χ^2
Annealed	5.657	3.61×10^{-5}	3.93×10^{-5}	0.751	0.928	1767	4615	1.09×10^{-3}
STA890	5.749	1.68×10^{-5}	2.05×10^{-5}	0.4677	0.9107	1203.4	4322	3.50×10^{-5}
STA920	6.054	1.56×10^{-5}	2.49×10^{-5}	0.5247	0.9234	746.3	4160	2.95×10^{-5}
STA950	4.201	1.50×10^{-5}	2.34×10^{-5}	0.609	0.965	44.06	3304	2.04×10^{-3}

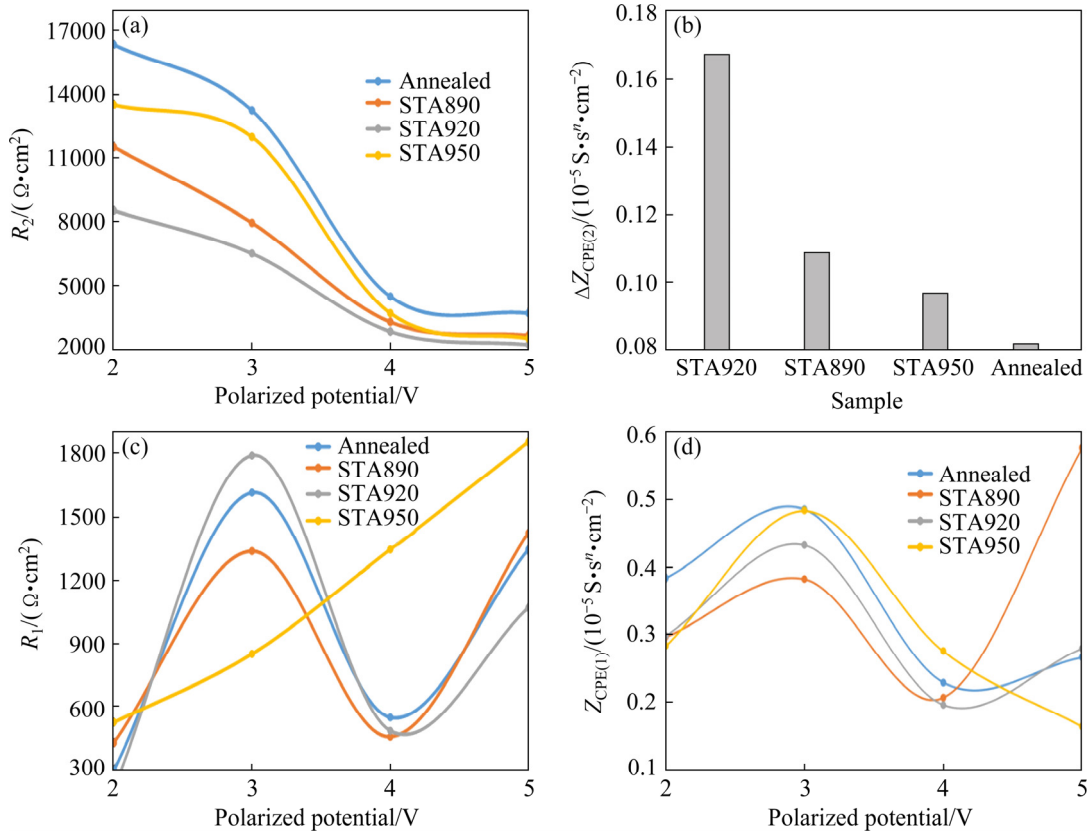

Fig. 9 Analysis on fitted parameters of potentiostatic polarization tests at 2, 3, 4 and 5 V: (a) R_2; (b) $\Delta Z_{CPE(2)}$; (c) R_1; (d) $Z_{CPE(2)}$

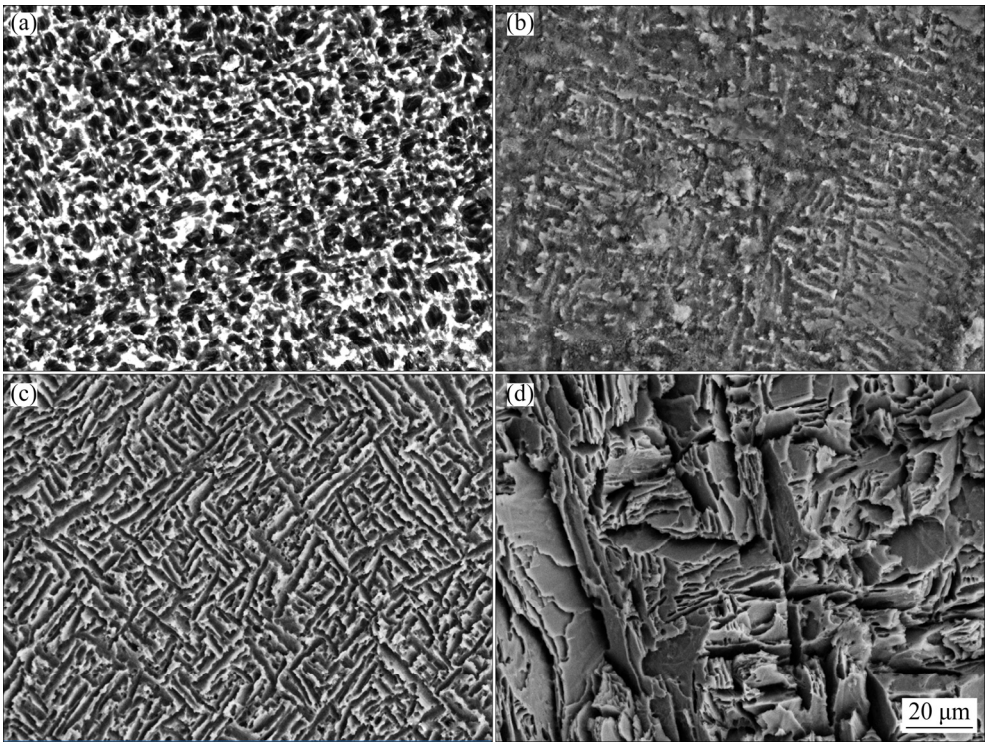

Fig. 10 Surface morphologies after transpassive dissolution for LAM Ti6Al4V samples: (a) Annealed; (b) STA890; (c) STA920; (d) STA950

accompanied with the lowest R_2 (Fig. 9(a)). However, STA950 sample representing the highest corrosion rate in the OCP condition can produce a thicker passivation film than STA890, leading to a slightly higher R_2, even both of them have more or less similar volume fraction and microstructure morphology of β phase. In conclusion, the corrosion rate after entering the passivation region relies on the dissolution rate of the passivation film, which is mainly determined by different phase distributions, especially for the difficult-to-dissolve phase that highly affects on the compactness and stability of the produced passivation film.

4.2 Corrosion performance in over-passivation dissolving region III

Figure 10 shows the surface morphology of the annealed and STA samples through transpassivation dissolution (Region III in Fig. 6). Comparatively, the annealed sample (Fig. 10(a)) dissolves smoothly due to its fairly uniform microstructure and element distributions, where a certain amount of deep holes illustrate that the dissolution initiates from the α_p phase. The difference in the dissolution rates of the Al-rich α_p and the V-rich β_{trans} is enlarged with the increment of the volume fraction of the β_{trans} colony. It is identified that the α_p and α_s inside the β_{trans} colony dissolve to deep grooves. In addition, the dissolution rates in the transpassivation region III are consistent with the rank in the active region I. Because the dense or thick passivation film is not capable to be produced in this region, the Ti6Al4V dissolution rate is accelerated distinctly during electrochemical machining process. Controlled by the element segregation and inconsistent dissolution rate of different phases, the electrochemical machining parameters should be paid attention and well optimized in order to guarantee the surface quality.

5 Conclusions

(1) The microstructure morphology shows clear differences between the annealed and STA samples, especially for the volume fraction of β_{trans} that is increased with the solution temperature. The STA treatment aggravates the element micro-segregation compared to the annealing treatment. It is proven that either Al-rich or V-rich condition can highly affect the electrochemical dissolution behaviors.

(2) The dissolution rates of the samples under

the OCP and metastable passivation conditions show different orders from the potentiostatic polarization condition. The former is determined by the thermodynamical instability caused by element micro-segregation. The latter is virtually controlled by the stability of the produced film that is highly affected by the phase distributions, especially for the difficult-to-dissolve phase that highly affects the compactness of the film.

(3) Surface morphology of transpassivation dissolution of the annealed and STA samples shows that the dissolution difference between the primary Al-rich α phase and the V-rich β_{trans} structure is enlarged with the volume fraction of the β_{trans} colony increasing. The dissolution rates in the transpassivation region are consistent with the rank in the active region, because the dense or thick passivation film is not capable of being produced.

Acknowledgments

The authors are grateful for the financial supports from the project of Ministry of Industry and Information Technology of China (No. 2019-00899-1-1), the Natural Science Foundation of Shaanxi Province, China (No. 2021JM-060), and Fundamental Research Funds for the Central Universities, China (No. 3102019QD0409).

References

[1] THIJS L, VERHAEGHE F, CRAEGHS T, HUMBEECK J V, KRUTH J P. A study of the micro structural evolution during selective laser melting of Ti6Al4V [J]. Acta Materialia, 2010, 58: 3303−3312.

[2] YANG Liu-qing, YANG Yan-qing. Deformed microstructure and texture of Ti6Al4V alloy [J]. Transactions of Nonferrous Metals Society of China, 2014, 24(10): 3103−3110.

[3] LIN Xin, HUANG Wei-dong. Laser additive manufacturing of high-performance metal components [J]. Science China, 2015, 45(9): 1111−1126.

[4] LIN Xin, HUANG Wei-dong. High performance metal additive manufacturing technology applied in aviation field [J]. Materials China, 2015, 34(9): 684−688.

[5] ZHAO Zhuang, CHEN Jing, ZHANG Qiang, TAN Hua, LIN Xin, HUANG Wei-dong. Microstructure and mechanical properties of laser additive repaired Ti17 titanium alloy [J]. Transactions of Nonferrous Metals Society of China, 2017, 27(12): 2613−2621.

[6] GUO Peng-fei, LIN Xin, REN Yong-ming, XU Jian-jun, LI Jia-qiang, ZHANG Yu-feng, CHEN Jing, HUANG Wei-dong. Microstructure and electrochemical anodic behavior of Inconel 718 fabricated by high-power laser solid forming [J]. Electrochimica Acta, 2018, 276: 247−260.

[7] GUO Peng-fei, LIN Xin, HUANG Wei-dong. Columnar structure and electrochemical anisotropy of a nickel-based superalloy fabricated via laser solid forming [J]. Journal of Applied Electrochemistry, 2017, 47: 1083−1090.

[8] GUO Peng-fei, LIN Xin, ZHANG Yu-feng, LI Jia-qiang, XU Jian-jun, REN Yong-ming, LIU Jian-rui, YANG Hai-ou, HUANG Wei-dong. Distinction in anodic dissolution behavior of Inconel 718 prepared by different forming technologies [J]. Journal of the Electrochemical Society, 2018, 165(11): 546−555.

[9] WANG Xin-di, QU Ning-song, GUO Peng-fei, FANG Xiao-long, LIN Xin. Electrochemical machining properties of the laser rapid formed Inconel718 alloy in $NaNO_3$ solution [J]. Journal of the Electrochemical Society, 2017, 164(14): 548−559.

[10] ATAPOUR M, PILCHAK A, FRANKEL G S, WILLIAMS J C, FATHI M H, SHAMANIAN M. Corrosion behavior of Ti6Al4V with different thermomechanical treatments and microstructures[J]. Corrosion, 2010, 66: 0650046.

[11] GEETHA M, MUDALI U K, GOGIA A K, ASOKAMANI R, RAJ B. Influence of microstructure and alloying elements on corrosion behavior of Ti13Nb13Zr alloy [J]. Corrosion Science, 2004, 46: 877−892.

[12] DAI Nian-wei, ZHANG Lai-chang, ZHANG Jun-xi, CHEN Qi-meng, WU Mao-liang. Corrosion behavior of selective laser melted Ti6Al4V alloy in NaCl solution [J]. Corrosion Science, 2016, 102: 484−489.

[13] LI Jia-qiang, LIN Xin, ZHENG Min, WANG Jian, GUO Peng-fei, QIN Tuo, ZHU Ming-hui, HUANG Wei-dong, YANG Hai-ou. Distinction in anodic dissolution behavior on different planes of laser solid formed Ti6Al4V alloy [J]. Electrochimica Acta, 2018, 283: 1482−1489.

[14] LI Jia-qiang, LIN Xin, GUO Peng-fei, SONG Meng-hua, HUANG Wei-dong. Electrochemical behavior of laser solid formed Ti6Al4V alloy in a highly concentrated NaCl solution [J]. Corrosion Science, 2018, 142: 161−174.

[15] ZHANG Shuang-yin, LIN Xin, CHEN Jing, HUANG Wei-dong. Heat-treated microstructure and mechanical properties of laser solid forming Ti6Al4V alloy [J]. Rare Metals, 2009, 28: 537−544.

[16] YAO Jin, SUO Tao, ZHANG Shuang-yin, ZHAO Feng, WANG Hong-tao, LIU Jia-bin, CHEN Yu-zeng, LI Yu-long. Influence of heat-treatment on the dynamic behavior of 3D laser-deposited Ti6Al4V alloy [J]. Materials Science and Engineering A, 2016, 677: 153−162.

[17] REN Yong-ming, LIN Xin, FU Xin, TAN Hua, CHEN Jing, HUANG Wei-dong. Microstructure and deformation behavior of Ti−6Al−4V alloy by high-power laser solid forming [J]. Acta Materialia, 2017, 132: 82−95.

[18] LI Jia-qiang, LIN Xin, WANG Jian, ZHENG Min, GUO Peng-fei, ZHANG Yu-feng, REN Yong-ming, LIU Jian-rui, HUANG Wei-dong. Effect of stress-relief annealing on anodic dissolution behaviour of additive manufactured Ti−6Al−4V via laser solid forming [J]. Corrosion Science, 2019, 153: 314−326.

[19] SHARMA G, RAMAMUJAN R V, TIWARI G P. Instability mechanisms in lamellar microstructures [J]. Acta Materialia, 2000, 48: 875−889.

[20] WU Bin-tao, PAN Zeng-xi, LI Si-yuan, CUIURI D, DING Dong-hong, LI Hui-jun. The anisotropic corrosion behavior

of wire arc additive manufactured Ti6Al4V alloy in 3.5% NaCl solution [J]. Corrosion Science, 2018, 137: 176−183.
[21] MILOSEV I, KOSEC T, STREHBLOW H H. XPS and EIS study of the passive film formed on orthopaedic Ti6Al7Nb alloy in Hank's physiological solution [J]. Electrochimica Acta, 2008, 53: 3547−3558

元素偏析和相分布控制的激光增材制造 Ti6Al4V 合金的电化学溶解与钝化

于 君[1,2]，覃 拓[3]，林 鑫[1,2]，王俊杰[1]，张宇锋[1,2]，王诗尧[1]，杨静怡[1,2]，黄卫东[1,2]

1. 西北工业大学 凝固技术国家重点实验室，西安 710072；
2. 西北工业大学 金属高性能增材制造与创新设计工业和信息化部重点实验室，西安 710072；
3. 中国航天科技集团公司第九研究院 微电子技术研究所，西安 710119

摘 要：采用 Tafel 极化、恒电位极化和交流阻抗测试研究激光增材制造 Ti6Al4V 合金的电化学溶解和钝化。结果表明，与退火处理相比，固溶时效(STA)加剧元素的微观偏析，导致不同样品中相的 Al 和 V 含量不同。由元素偏析导致的热力学不稳定性决定富 Al 或富 V 条件对相的电化学溶解行为有显著影响。亚稳钝化过程中的溶解速率是由生成膜的稳定性控制，该稳定性受相分布的影响显著，尤其是难溶解相。在过钝化区中合金表面不能产生致密的钝化膜，因此，相的溶解速率与活化过程排序一致。与退火试样相比，STA 试样具有较高的溶解速率，有利于 Ti6Al4V 的电解加工。

关键词：激光增材制造；电化学溶解行为；显微组织特征；电流效率；Ti6Al4V 合金

(Edited by Bing YANG)